Lightweight Human-Friendly Robotic Arm based on Transparent Hydrostatic Transmissions

Marco Bolignari, Gianluca Rizzello, Luca Zaccarian, Marco Fontana

Lightweight Human-Friendly Robotic Arm based on Transparent Hydrostatic Transmissions

Marco Bolignari[1,4], Gianluca Rizzello[2], Luca Zaccarian[3,4], Marco Fontana[1]

***Abstract*—We present theoretical and experimental results pertaining the development and the control of a two-link robotic arm with remotized actuation via rolling diaphragm hydrostatic transmissions. We develop a dynamical model capturing the essential dynamics of the developed transmission/robot ensemble and propose a control strategy consisting in two nested loops, the inner one performing high-bandwidth joint torque regulation and the outer one implementing various types of compliance mechanisms for effective human-robot interactions. An extensive experimental campaign testing both the low-level torque controller and the high-level compliance controller confirms the effectiveness of the proposed hardware-software remotization architecture.**

I. Introduction

Modern robots are progressively spreading in our society, and several aspects of human life are increasingly being supported by robotic devices. When developing robots that interact with humans, safety is certainly among the main requirements, however suitable levels of performance must also be guaranteed. Conventional robots are intrinsically unsafe due to their high-impedance actuators (i.e. electric motors coupled with gearboxes) but they can be made safe introducing sensors and active impedance controllers, however this comes to a cost, i.e. a strong limitations in performance in terms of speed and high frequency bandwidth [1].

To effectively overcome this trade-off, novel hardware design paradigms have been proposed, where the demanded safety and performance are directly embedded within the intrinsic open-loop response of purposely conceived smart mechanical architectures. As an example, Series Elastic Actuators (SEA) employ compliant drivetrains to dynamically decouple the inertia of the actuators and links [2], resulting in safe operations over a broad range of frequencies. However, this design solution inherently limits the control bandwidth and performance. To overcome this drawback, SEA evolved in Variable Stiffness Actuator (VSA) [3]. Nevertheless, hardware solutions for stiffness modulation increases the complexity, the encumbrance, and the mass.

Manuscript received: .... ; Revised ....; Accepted .....

This work was supported by MIUR under the Program Department of Excellence of Robotics and AI the Scuola Superiore Sant'Anna and of the DII of University of Trento.

[1] Institute of Mechanical Intelligence, Scuola Superiore Sant'Anna, Pisa, 56100, Italy ⟨marco.bolignari,marco.fontana⟩@santannapisa.it

[2]Dept. of Systems Engineering, Saarland University, Saarbrücken, DE 66123 Germany gianluca.rizzello@imsl.uni-saarland.de

[3] LAAS-CNRS, Université de Toulouse,CNRS, Toulouse, France.

[4]Department of Industrial Engineering, University of Trento, Trento 38123, Italy luca.zaccarian@unitn.it

Digital Object Identifier (DOI): see top of this page.

An effective solution to address the trade-off between safety and performance is offered by remotization strategies, where the actuators are placed far from the joint axes, e.g., at the robot base, and power transmission systems are used to transfer the torque from the base actuators to the actuated joints. This solution provides different improvements: 1) the moving elements of the resulting robotic structure are extremely lightweight; 2) the actuators' mass is not a parameter to be minimised any longer, and low-inertia direct-drive (or quasi direct-drive) actuators can be employed reducing stored kinetic energy and consequently minimizing the injury hazard in the event of non-predicted collisions; 3) performance of the robotic system is improved in terms of speed and dynamic bandwidth. Steel-cable/pulley transmissions have been extensively as a mean of remotization because of their efficiency, lightweight, and reduced encumbrance [4]–[6]. However, the complexity of cable routing is high and it largely increases with the number of degrees of freedom. Moreover, the need for deviating heavy-loaded cables about a multitude of pulleys generally introduces compliance in the transmission that limits the closed-loop torque-control bandwidth. Alternatively, bowden cables can be employed effectively reducing the system complexity and cost, but performance is penalized, being affected by high friction that produces wear, limited bandwidth and poor mechanical transparency/backdrivability.

Recently, Rolling Diaphragm Hydrostatic Transmissions (RDHT) have been conceived as an attractive solution for remotization, which offers a combination of desirable features for designing lightweight high-bandwidth cost-effective robotic devices. RDHT have been employed to develop passive telepresence systems [7], robots for extending the reach inside MRI bores [8] and similar MRI compatible devices [9], [10], upper-limb [11], lower-limb [12], [13] exoskeletons, wearable supernumerary arms [14], [15] and legs [16], as well as robotic grippers [17] and agile legged robots [18]. RDHTs embody the gentle-yet-powerful paradigm by combining high specific-torque and stiffness of hydraulic systems, with the ease in controlling of electric actuators. Static friction and backlash can be conveniently cancelled by using rolling diaphragm cylinders in antagonistic configuration [19]. Viscous friction is conveniently independent of the transmitted torque [20]. Large manufacturing tolerances and low-cost production make the RDHT solution an ideal paradigm for developing human-friendly robotic arms. Finally, the measurement of the output torque by means of pressure sensors is a cost-effective strategy that produces high accuracy and large torque-control bandwidth when used as feedback signal [21].

Despite recent achievements, rigorous control strategies

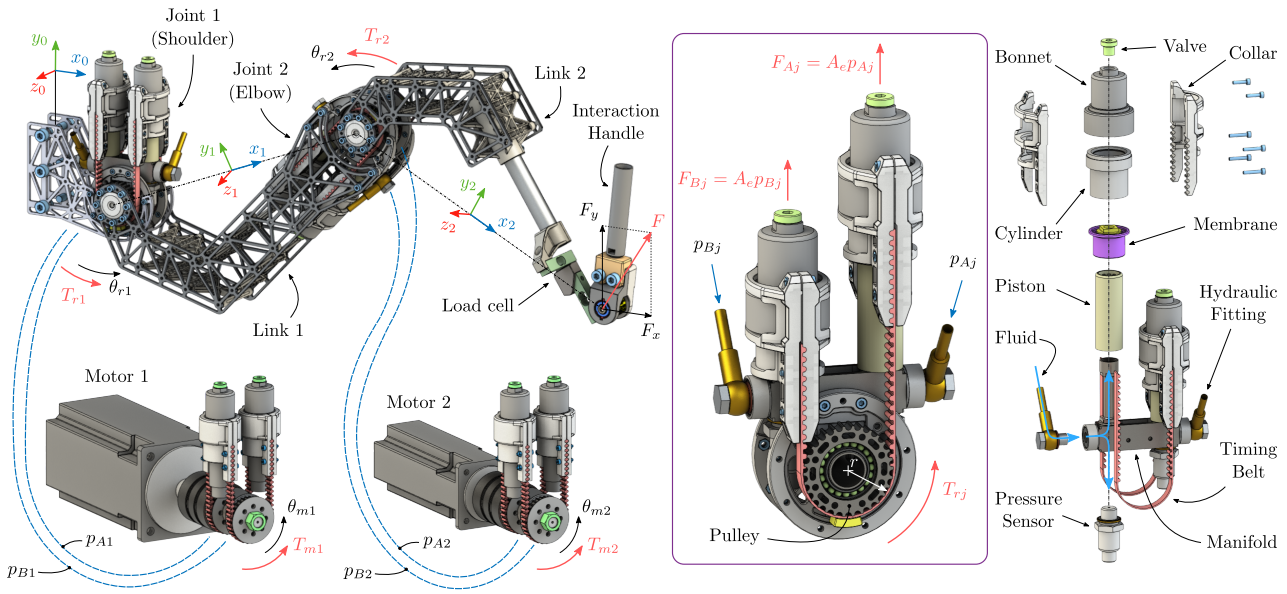

Fig. 1. Experimental prototype of the lightweight robotic arm. *Left:* overall system; blue dashed lines represent the hydraulic hoses. *Center:* Integrated robotic joint based on rolling diaphragm hydrostatic cylinders with floating-bonnet layout. *Right:* Detailed view of the robotic joint, describing constructive details and the internal distribution of the fluid.

for multi-DOF RDHT-based collaborative robots with remote direct or quasi-direct drive actuation has not been developed yet. Moreover, experimental characterization of the interactive features of hydrostatic robotic arms has been marginally addressed. Only preliminary studies on a single DoF robotic arm have been conducted by the authors of this manuscript [21].

Here, as compared to [21], we abandon the need of Smith-predictor solution, due to improvements on our hardware devices, and we address the more challenging nonlinear problem associated to a two-link robotic arm. In particular, we present the design and interaction control of a prototype of a lightweight, planar collaborative robotic arm actuated by hydrostatic transmissions. The force-controlled open-loop response of the robot (obtained by relying on the motor-side current loops executed by the motor drivers) is initially analysed, and a simplified dynamical model characterizing the essential dynamical structure of hydrostatic robotic arms is proposed. To ensure effective regulation of the mechanical interaction at the robot end-effector, a novel hierarchical closed-loop control architecture is proposed for the considered class of systems. First, a model-based low-level torque controller is studied and applied to each transmission line. The high-bandwidth low-level controller is solely based on pressure sensing feedback, and ensures tight regulation of the torque transmitted to the robot joints, while suppressing oscillatory dynamics and enhancing backdrivability. Then, the low-level torque controllers are nested within a high-level human-robot interaction controller, whose goal is the regulation of the overall robot interaction (i.e., stiffness and damping) in the operating space. The benefit of this architecture consists in the possibility of easily controlling the robot treating the hydrostatically-actuated joints as ideal sources of torque. An extensive experimental campaign well illustrates the safety and accuracy of the prototype under several different human-robot-interaction situations, such as heavy load tasks, low or high frequency tests and virtual viscous/elastic resistance rendering experiments.

The paper is organized as follows. In Sect. II, the novel rolling diaphragm hydrostatic transmission is presented, alongside its integration in the robotic arm. Sect. III and Sect. IV deal with low-level torque control and high-level interaction control, respectively. An extensive experimental validation campaign of the controlled system is then conducted in Sect. V, followed by concluding remarks in Sect. VI.

II. Rolling Diaphragm Hydrostatic Transmission Lightweight Arm

A. Design and Operating Principle

Fig. 1 (left) shows the lightweight robotic arm developed in this work. It consists of a 2-DOF planar manipulator, where rolling diaphragm hydrostatic transmissions are implemented to remotize the two electric motors, which are placed at the robot base. Fig. 1 (top-left) shows a handle placed at the end-effector, which allows interacting with a human user during the experiments (see Sect. V). A load cell placed on the handle measures the interaction force $F = [F_x, F_y]^\top$ between the human operator and the robot. This sensor is only used here for validation purposes, without being involved in the force control feedback, which is only based on low-cost pressure sensors placed at robot joints. As shown in Fig. 1 (left), each transmission system connects the j-th robotic joint ($j = 1$ referring to the "shoulder" joint, and $j = 2$ referring to the "elbow" joint) with the j-th motor and comprises two fluid lines equally pressurized at the rest conditions, i.e., $p_{Aj} = p_{Bj} = p_0$. When a positive torque T_{mj} is generated by the j-th motor, pressure p_{Aj} increases and pressure p_{Bj}, thus generating a differential pressure $\Delta p_j = p_{Aj} - p_{Bj}$ that

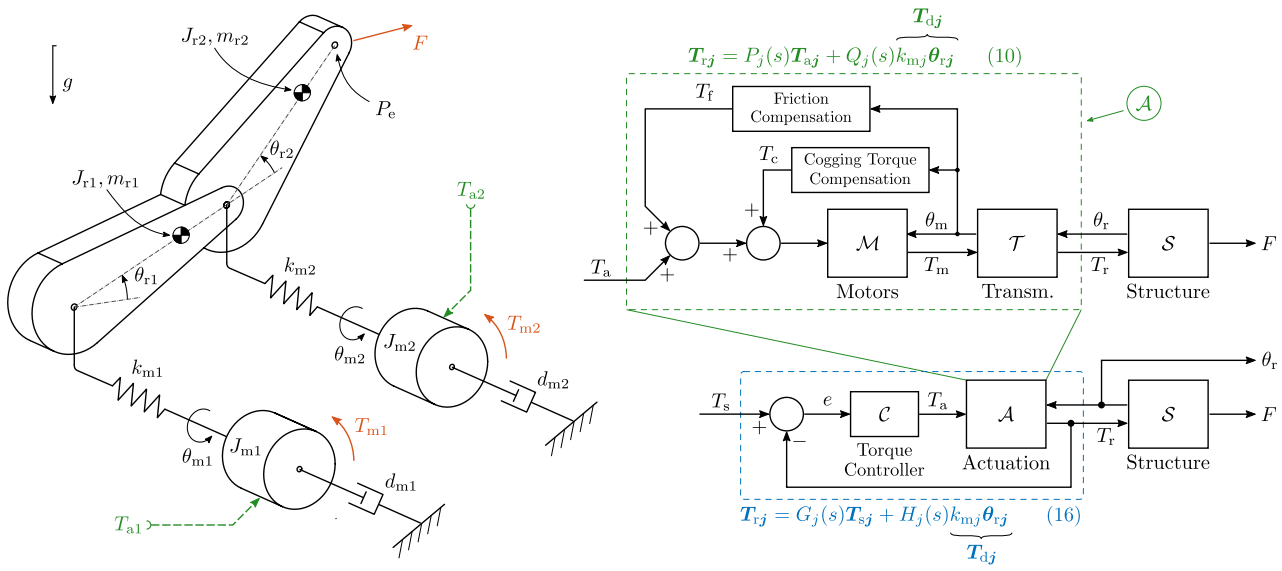

Fig. 2. *Left:* model of the precompensated robotic arm according to (4). *Right:* block-diagram representation of the precompensated actuators (in green) and the low-level torque-control scheme (in blue).

propagates through the fluid lines up to the robotic joint, where two output cylinders convert it back into torque T_{rj} exerted on the joint axis. Under ideal or static conditions, we have $T_{rj} \approx T_{mj}$. This equality, however, degrades when operating far from the static case due to viscous friction and dynamic effects, i.e., resonant modes, that become relevant at high operating frequencies. Improved accuracy is obtained here by sensing the transmitted torque T_{rj} by means of the above-mentioned pressure sensors placed on the fluid lines close to the robot joint, and closing a low-level (joint-level) torque feedback loop.

B. Hydrostatic Robotic Joint

Fig. 1 (center) shows the proposed hydrostatic robotic joint, and illustrates the pressure-to-torque transformation that takes place at the robot axes (the same transformation takes place at the input side, being the transmission symmetric). Two cylinders are coupled in an antagonistic configuration by two timing belts, which are routed around two output toothed pulleys. Each cylinder produces a linear force, proportional to its internal pressure and equivalent area A_e, on its corresponding belt branches:

$$F_{Aj} = A_e p_{Aj}, \quad F_{Bj} = A_e p_{Bj}. \tag{1}$$

When pressures p_{Aj} and p_{Bj} coincide, the two cylinders are balanced and no torque is generated on the pulley. When the two pressures are different, instead, a net torque is expected at the joint, equal to:

$$T_{rj} = r(F_{Aj} - F_{Bj}) = rA_e\Delta p_j, \tag{2}$$

where constant r is the pulley radius. When filled with incompressible fluids, e.g., water, the transmissions achieve high stiffness and synchronous motion between the motor and joint rotations, i.e., $\theta_{rj} \approx \theta_{mj}$. In practice, some compliance exists along the hydraulic lines due to the presence of dissolved air and the elasticity of the hoses, belts, and diaphragms. Therefore, this approximated kinematic relation among the two angles holds as long as the transmitted torque is reasonably small, and the operating frequency is significantly smaller than the first resonant mode.

The major novelty of the proposed design consists of the "manifold" element, connecting pistons, pressure sensors, and hydraulic hoses in a compact shape. This element has both structural and hydraulic properties. It undergoes the reaction forces of the two pistons, pushed by the fluid pressure, and the shaft, pulled by the tension forces of the belts. On the other hand, the its internal shape distributes the fluid coming from the hydraulic hoses to cylinders and pressure sensors. The manifold enables the placement of pressure sensors in close proximity of the cylinder chambers in order to measure joint torques T_{rj} through pressure measurements, as shown in (2), with high sensing bandwidth and accuracy. Sensing accuracy and mechanical transparency are further enhanced using rolling diaphragm cylinders with floating-bonnet layout developed in [20], to prevent sliding and static friction.

C. Robotic Arm Technical Specifications

The integrated robotic joint proposed in this work and shown in Fig. 1 (center and right) has an angular range of 140°, weighs 700 g, and has been tested with torque loads up to 20 Nm. The integrated joint is conceived as modular element, so that the same optimized design and dimensions are usable for all the robot joints. The cylinders are equipped with a *OA-106-145* rolling diaphragm from DiaCom Corp., characterized by an effective area $A_e = 510$ mm^2, a cylinder diameter 27 mm, a stroke 56.8 mm, and a 25 bar maximum working pressure. Timing belts are routed around two output toothed pulleys, with primitive radius $r = 23.9$ mm. The joint angular position θ_{rj} is measured by means of a RM08D01-12 magnetic incremental encoder from RLS (4096 cpr resolution),

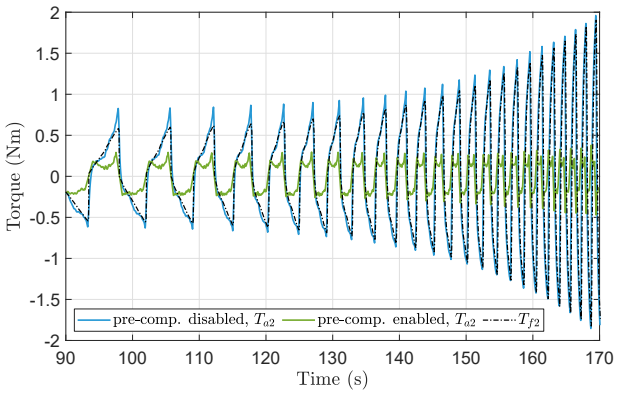

Fig. 3. Characterisation and feed-forward compensation of the transmission friction

while the fluid pressures p_{Aj} and p_{Bj} are measured by means of two 3100x pressure sensors from Gems Sensors (16 bar maximum pressure measurement and 0.04 bar accuracy). The hydraulic hoses, characterised by a flexible coating of Kevlar fibers, have a length of 1 m and an internal diameter of 5 mm; distilled water is used as working fluid. Two direct-drive motors AM8043 (4.90 Nm rated torque, 28.0 Nm peak torque) and AM8053 (14.9 Nm rated torque, 53.1 Nm peak torque) from Beckhoff are used for the actuation of elbow and shoulder joints, respectively. Both motors are equipped with a 24 bit (20 bit per revolution) multi-turn absolute encoder, which measures the motor position θ_{mj}. The control unit consists in a CX51 Beckhoff Embedded-PC based on a TwinCAT real-time communication protocol. All of the experiments showed in this work are performed with a fixed sampling rate of 2 kHz.

III. Modeling and Low-level Controller

This section presents a dynamical model of the robot-transmission ensemble, schematically represented in Fig. 2 (left), together with two model-based low-level control loops shown in Fig. 2 (right). The resulting low-level control action is then nested in a high-level feedback loop using the setpoint input T_s to modulate the virtual stiffness and damping response in the operational space. The overall scheme offers desirable human-robot-interaction features, as discussed later in Sect. IV.

A. Cogging Torque and Friction Compensation

Differently from the vast majority of robots, the mechanical transparency of the proposed architecture enables both open-loop (relying on the current-loop executed in the motor drivers) and closed-loop (relying on the pressure sensing of the transmission fluid) force control of the robot. Since the open-loop configuration enhances simplicity but lacks the capability of rejecting disturbances, an explicit compensation of the disturbance effects affecting the motor and the transmission lines assume a relevant role in our work.

A first precompensation action of the motor-transmission units, namely blocks $\mathcal{M}$ and $\mathcal{T}$, is shown in the green block $\mathcal{A}$ of Fig. 2 (right), comprising:

- the motor cogging torque compensation term $T_\mathrm{c} = [T_{\mathrm{c}1}(\theta_{\mathrm{m}1}), T_{\mathrm{c}2}(\theta_{\mathrm{m}2})]^\top$, which emerges from the off-line tuning experiments reported in [20], [21] performed after detaching the motor from the mechanical structure;
- the motor-transmission friction compensation term $T_\mathrm{f} = \left[T_{\mathrm{f}1}(\theta_{\mathrm{m}1}, \dot\theta_{\mathrm{m}1}), T_{\mathrm{f}2}(\theta_{\mathrm{m}2}, \dot\theta_{\mathrm{m}2})\right]^\top$, whose selection for each motor is described next.

Term T_f is determined by detaching the robot structure from the transmissions' output and performing motor position control following constant-velocity trajectories spanning the entire rotation range of the transmission, $\pm 65°$; the velocity is increased at each repetition from 0.1 rad/s to 3 rad/s. The torque input T_a required to follow the desired trajectory is shown by the blue line in Fig. 3 (*top*). At low speeds, small torque jumps when reversing the rotation direction indicate the presence of Coulomb friction contribution, while the linear trend over constant-velocity strokes highlights some weak linear spring-rate effect introduced by the membranes. At higher velocities, instead, viscous quadratic contributions become predominant. This combination of effects is characterised by fitting the experimental data with the following model

$$\begin{aligned} T_\mathrm{f}(\theta_\mathrm{m}, \dot\theta_\mathrm{m}) &= T_v(\dot\theta_\mathrm{m}) + T_e(\theta_\mathrm{m}) + T_u(\dot\theta_\mathrm{m}) = \\ &= c_v|\dot\theta_\mathrm{m}|\dot\theta_\mathrm{m} + c_e(\theta_\mathrm{m} - \theta_0) + b_\mathrm{f}\mathbf{sign}(\dot\theta_\mathrm{m}) \end{aligned} \tag{3}$$

where contributions T_v, T_e, and T_u represent the quadratic viscous term, the spring-rate term, and the Coulomb friction term, respectively. Constant θ_0 corresponds to the angular position where the intensity of the linear spring-rate effect is zero, while the remaining parameters are calibrated as follows: $c_v = 0.21$ Nm s^2/rad^2, $c_e = 0.28$ Nm/rad, $\theta_f = 0.047$ rad, $b_f = 0.28$ Nm. The resulting fit is shown by the black lines in Fig. 3. An effective compensation of the friction torque is achieved by adding the feed-forward term T_f to the torque reference commanded to the motor driver (see Fig. 2 (right)).

The compensation results are shown in Fig. 3 (*bottom*), reporting the motor torque needed to track the same characterisation trajectory after applying the friction compensation; the strategy revealed effective, especially at high velocities.

B. Modeling and Precompensated Actuation

The left and right pictures in Fig. 2 show a parallel between the physical modeling of the manipulator-transmission ensemble and the precompensated block $\mathcal{A}$. The physical system is described by the three main blocks in Fig. 2 (top-right):

- block $\mathcal{M}$ contains the dynamics of the motors (it also incorporates the current controller executed by the motor drivers) characterised by moment of inertia $J_{\mathrm{m}j}$, $j = 1, 2$, and generating the actuation torques $T_\mathrm{m} = [T_{\mathrm{m}1}, T_{\mathrm{m}2}]^\top$;
- block $\mathcal{T}$ represents the transmission system in terms of spring, with stiffness $K_\mathrm{m} = \mathrm{diag}(k_{\mathrm{m}1}, k_{\mathrm{m}2}) > 0$, and linear dampers, characterized by coefficients $D_\mathrm{m} = \mathrm{diag}(d_{\mathrm{m}1}, d_{\mathrm{m}2}) > 0$ which model the residual damping of the transmission (after the compensation described in Sect. III-A) according to an equivalent lumped description;
- finally, block $\mathcal{S}$ describes the dynamics of the arm structure, where parameters $m_{\mathrm{r}j}$ and $J_{\mathrm{r}j}$ describe the mass

and inertial properties of the links, $P_{\mathrm{e}} = [P_{\mathrm{e}x}, P_{\mathrm{e}y}]^\top$ defines the end-effector position in the workspace, which is a subset of the (x, y) plane, and $F = [F_x, F_y]^\top$ defines the force applied by the robot on the surrounding environment at position P_{e}.

The motors are rigidly connected to the transmission inputs, while the output side of the transmissions are rigidly connected to the links of the arm. These interconnections can be described as force-position feedbacks, where the coupling between $\mathcal{M}$ and $\mathcal{T}$ is described by the motor torques $T_{\mathrm{m}} = [T_{\mathrm{m}1}, T_{\mathrm{m}2}]^\top$ and the motor positions $\theta_{\mathrm{m}} = [\theta_{\mathrm{m}1}, \theta_{\mathrm{m}2}]^\top$, while the coupling between $\mathcal{T}$ and $\mathcal{S}$ is described by the joint torques $T_{\mathrm{r}} = [T_{\mathrm{r}1}, T_{\mathrm{r}2}]^\top$ and the joint positions $\theta_{\mathrm{r}} = [\theta_{\mathrm{r}1}, \theta_{\mathrm{r}2}]^\top$.

After applying the cogging-torque and the friction-torque compensations T_c and T_f, described in Sect. III-A, the equations of motion can be expressed as follows:

$$\begin{aligned}&\begin{bmatrix} M_{\mathrm{m}} & 0 \\ 0 & M_r(\theta_{\mathrm{r}}) \end{bmatrix} \begin{bmatrix} \ddot{\theta}_{\mathrm{m}} \\ \ddot{\theta}_{\mathrm{r}} \end{bmatrix} + \begin{bmatrix} D_{\mathrm{m}} & 0 \\ 0 & D_{\mathrm{r}} \end{bmatrix} \begin{bmatrix} \dot{\theta}_{\mathrm{m}} \\ \dot{\theta}_{\mathrm{r}} \end{bmatrix} + \\ &\begin{bmatrix} K_{\mathrm{m}} & -K_{\mathrm{m}} \\ -K_{\mathrm{m}} & K_{\mathrm{m}} \end{bmatrix} \begin{bmatrix} \theta_{\mathrm{m}} \\ \theta_{\mathrm{r}} \end{bmatrix} + \begin{bmatrix} 0 \\ C_r(\theta_{\mathrm{r}}, \dot{\theta}_{\mathrm{r}})\dot{\theta}_{\mathrm{r}} + G_{\mathrm{r}}(\theta_{\mathrm{r}}) \end{bmatrix} = \\ &\begin{bmatrix} I \\ 0 \end{bmatrix} T_a + \begin{bmatrix} 0 \\ J^\top(\theta_{\mathrm{r}}) \end{bmatrix} F,\end{aligned} \tag{4}$$

where M_{m} and $M_{\mathrm{r}}(\theta_{\mathrm{r}})$ are the inertia matrices associated with the motors and the robot, respectively, D_{m} and D_{r} are the corresponding damping matrices, and K_m is the stiffness matrix associated with the coupling. Matrices $C_{\mathrm{r}}(\theta_{\mathrm{r}}, \dot{\theta}_{\mathrm{r}})\dot{\theta}_{\mathrm{r}}$ and $G_{\mathrm{r}}(\theta_{\mathrm{r}})$ collect the Coriolis and gravity effects, and J is the Jacobian matrix of the robot arm [22]. Subscripts "m" and "r" refer to the motor unit, namely $\mathcal{M}$ and $\mathcal{T}$, and robotic structure $\mathcal{S}$, respectively. Variable $T_{\mathrm{a}} = [T_{\mathrm{a}1}, T_{\mathrm{a}2}]^\top$, which collects the desired joint torques of the precompensated system, is the control input of the green block $\mathcal{A}$ in Fig. 2.

C. Torque Dynamics Analysis

To suitably represent dynamics (4), we introduce the following change of coordinates (which is always well-defined, since $K_{\mathrm{m}} > 0$):

$$\begin{bmatrix} T_{\mathrm{r}} \\ \theta_{\mathrm{r}} \end{bmatrix} = \begin{bmatrix} K_{\mathrm{m}} & -K_{\mathrm{m}} \\ 0 & I \end{bmatrix} \begin{bmatrix} \theta_{\mathrm{m}} \\ \theta_{\mathrm{r}} \end{bmatrix}, \tag{5}$$

and, by replacing (5) in (4), we obtain:

$$\begin{aligned}&\begin{bmatrix} M_{\mathrm{m}}K_{\mathrm{m}}^{-1} & M_{\mathrm{m}} \\ 0 & M_{\mathrm{r}}(\theta_{\mathrm{r}}) \end{bmatrix} \begin{bmatrix} \ddot{T}_{\mathrm{r}} \\ \ddot{\theta}_{\mathrm{r}} \end{bmatrix} + \begin{bmatrix} D_{\mathrm{m}}K_{\mathrm{m}}^{-1} & D_{\mathrm{m}} \\ 0 & D_{\mathrm{r}} \end{bmatrix} \begin{bmatrix} \dot{T}_{\mathrm{r}} \\ \dot{\theta}_{\mathrm{r}} \end{bmatrix} + \\ &\begin{bmatrix} I & 0 \\ -I & 0 \end{bmatrix} \begin{bmatrix} T_{\mathrm{r}} \\ \theta_{\mathrm{r}} \end{bmatrix} + \begin{bmatrix} 0 \\ C_{\mathrm{r}}(\theta_{\mathrm{r}}, \dot{\theta}_{\mathrm{r}})\dot{\theta}_{\mathrm{r}} + G_{\mathrm{r}}(\theta_{\mathrm{r}}) \end{bmatrix} = \\ &\begin{bmatrix} I \\ 0 \end{bmatrix} T_{\mathrm{a}} + \begin{bmatrix} 0 \\ J^\top(\theta_{\mathrm{r}}) \end{bmatrix} F.\end{aligned} \tag{6}$$

In these new coordinates, the transmitted torque T_{r} appears explicitly as a state variable. For each $j = 1, 2$, we may then expand the differential equations governing the state $T_{\mathrm{r}j}$ in scalar form, which gives:

$$\frac{J_{\mathrm{m}j}}{k_{\mathrm{m}j}}\ddot{T}_{\mathrm{r}j} + \frac{d_{\mathrm{m}j}}{k_{\mathrm{m}j}}\dot{T}_{\mathrm{r}j} + T_{\mathrm{r}j} = T_{\mathrm{a}j} - J_{\mathrm{m}j}\ddot{\theta}_{\mathrm{r}j} - d_{\mathrm{m}j}\dot{\theta}_{\mathrm{r}j}. \tag{7}$$

From the point of view of equation (7), $T_{\mathrm{a}j}$ is a control input and $T_{\mathrm{r}j}$ is the corresponding system output, while $\dot{\theta}_{\mathrm{r}j}$ and $\theta_{\mathrm{r}j}$ act as disturbances on the relationship between $T_{\mathrm{a}j}$ and $T_{\mathrm{r}j}$. This disturbance can be seen as a dynamic effect from the joint angle $\theta_{\mathrm{r}j}$ that is zero with constant angles and becomes increasingly important as the operation frequency increases. To better quantify the effects of disturbance $\theta_{\mathrm{r}j}$ on the transmitted torque dynamics, we may define a scaled disturbance torque $T_{\mathrm{d}j}$ according to

$$T_{\mathrm{d}j} = k_{\mathrm{m}j}\theta_{\mathrm{r}j}, \tag{8}$$

so that control input, output, and disturbance are dimensionally equivalent (i.e. they all correspond to torques). By replacing (8) in (7), taking the Laplace transform (bold letters indicate variables in the Laplace domain without indicating explicitly variable "s", i.e. $\boldsymbol{x} := \mathcal{L}[x(t)]$), and solving (7) for variable $\boldsymbol{T_{\mathrm{r}j}}$, we get:

$$\begin{aligned}\boldsymbol{T_{\mathrm{r}j}} &= \frac{\omega_j^2}{s^2 + 2\xi_j\omega_j s + \omega_j^2}\boldsymbol{T_{\mathrm{a}j}} - \frac{s(s + 2\xi_j\omega_j)}{s^2 + 2\xi_j\omega_j s + \omega_j^2}\boldsymbol{T_{\mathrm{d}j}} \\ &= P_j(s)\boldsymbol{T_{\mathrm{a}j}} + Q_j(s)\boldsymbol{T_{\mathrm{d}j}},\end{aligned} \tag{9}$$

where $\omega_j^2 = k_{\mathrm{m}j}/J_{\mathrm{m}j}$ and $\xi_j = c_{\mathrm{m}j}/(2J_{\mathrm{m}j}\omega_j)$ represent the natural frequency and the modal damping of the second-order transfer function $P_j(s)$ from $\boldsymbol{T_{\mathrm{a}j}}$ to $\boldsymbol{T_{\mathrm{r}j}}$, and transfer function $Q_j(s)$ describes the dynamic effect of disturbance $T_{\mathrm{d}j}$. We refer to (9), depicted in green in Fig. 2 (top-right), as the *open-loop* response, since it describes the system behavior when no torque feedback is applied. Fig. 4 (top) shows the experimental identification of transfer function $P_j(s)$, and Fig. 4 (center) shows the comparison between $P_j(s)$ and $Q_j(s)$ in the frequency domain for both of the hydrostatic transmissions of the 2-dof manipulator. By replacing $s = \jmath\omega$ in (9) and evaluating the low-frequency limit case, we obtain:

$$\boldsymbol{T_{\mathrm{r}j}} \approx \boldsymbol{T_{\mathrm{a}j}} - \jmath\left(2\xi_j\frac{\omega}{\omega_j}\right)\boldsymbol{T_{\mathrm{d}j}}. \tag{10}$$

Equation (10) reveals that the transmitted torque $T_{\mathrm{r}j}$ closely follows $T_{\mathrm{a}j}$ as long as the robot operates at relatively low frequencies with respect to the open-loop natural frequency ω_j. The dynamic disturbances $T_{\mathrm{d}j}$, caused by the coupling between the motor and the structure, become non negligible as the driving speed increases.

D. Low-level Closed-loop Torque Controller

Since in practice the open-loop values of ξ_j and ω_j may lead to unsatisfactory under-damped dynamic performance, we are interested in further improving the open-loop response (9) by closing the low-level feedback control loop in the blue block of Fig. 2 (right). To this end, we exploit the measurements of the joint torques $T_{\mathrm{r}j}$ provided by the pressure sensors discussed in Sect. II, as represented in the blue block of Fig. 2. We show below that the transfer function from $T_{\mathrm{s}j}$ (setpoint) to $T_{\mathrm{r}j}$ (exerted torque) can be arbitrarily shaped by the designer. Afterwards, we investigate the influence of disturbance $T_{\mathrm{d}j}$ of (8) on this closed-loop architecture.

The closed-loop torque controller $\mathcal{C}$ is decentralized:

$$\mathcal{C}(s) = \begin{bmatrix} C_1(s) & 0 \\ 0 & C_2(s) \end{bmatrix}, \tag{11}$$

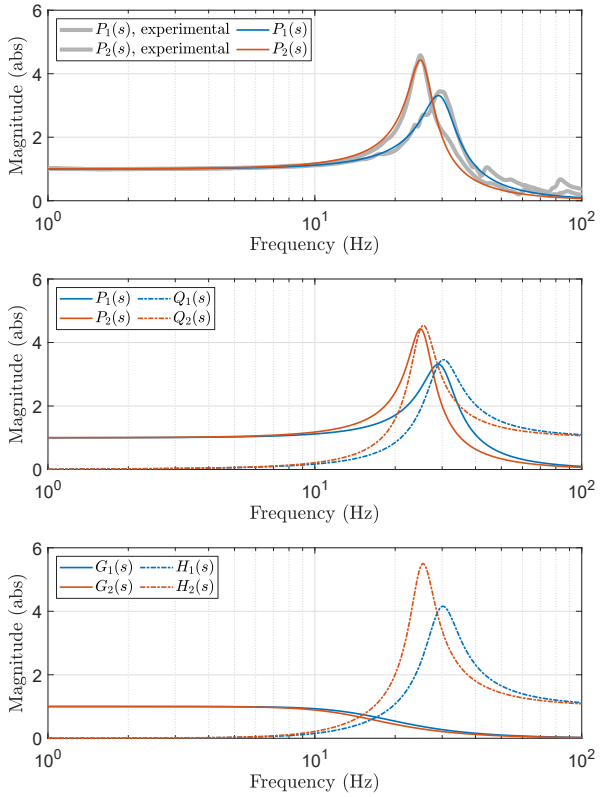

Fig. 4. Response of shoulder and elbow transmissions in the frequency domain. *Top:* experimental identification of the open-loop transfer functions $P_j(s)$ in (9). The experimental data are produced by fixing the end-effector to the ground and commanding T_{aj} in the form of chirp functions. The identified dynamical parameters in (9) correspond to $\xi_1 = 0.15$, $\omega_1 = 29.7$ Hz, $\xi_2 = 0.11$ and $\omega_2 = 25.2$ Hz. *Center:* analytical analysis of the open-loop transfer functions $P_j(s)$ and $Q_j(s)$. *Bottom:* analytical analysis of the closed-loop transfer functions $G_j(s)$ and $H_j(s)$, corresponding to the following selection of the free design parameters in (14): $\xi_{t1} = \sqrt{2}/2$, $\omega_{t1} = 16$ Hz, $\xi_{t2} = \sqrt{2}/2$ and $\omega_{t2} = 14$ Hz (imposing $G_j(s)$ critically damped).

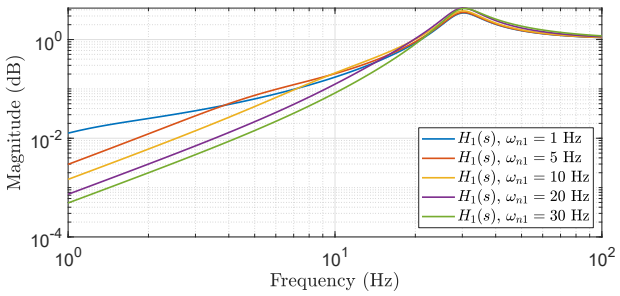

Fig. 5. Parametric analysis of transfer function $H_1(s)$ in (15) with different choices of parameter ω_{t1}. Parameter ξ_{t1} is always selected as $\sqrt{2}/2$ to achieve a critically-damped response. The (identified) plant parameters are $\xi_1 = 0.15$, $\omega_1 = 29.7$ Hz. The analysis of joint 2 would show the same trends and is not represented in the picture.

in order to act separately on each transmission line as follows:

$$\boldsymbol{T}_{\mathrm{a}\boldsymbol{j}} = C_j(s)\boldsymbol{e}_{\boldsymbol{j}} = C_j(s)\left(\boldsymbol{T}_{\mathrm{s}\boldsymbol{j}} - \boldsymbol{T}_{\mathrm{r}\boldsymbol{j}}\right), \ j = 1, 2. \tag{12}$$

The structure of $P_j(s)$ in (9) suggests to choose $C_j(s)$ in the form of filtered PIDs, [21], based on arbitrary time constants $\tau_{\mathrm{d}j}, j = 1, 2$:

$$C(s) = k_{\mathrm{p}j} + \frac{k_{\mathrm{i}j}}{s} + \frac{k_{\mathrm{d}j}s}{\tau_{\mathrm{d}j}s + 1} = \frac{\bar{k}_{\mathrm{d}j}s^2 + \bar{k}_{\mathrm{p}j}s + \bar{k}_{\mathrm{i}j}}{s\left(\tau_{\mathrm{d}j}s + 1\right)} \tag{13}$$

with $\bar{k}_{\mathrm{d}j} = k_{\mathrm{d}j} + k_{\mathrm{p}j}\tau_{\mathrm{d}j}$, $\bar{k}_{\mathrm{p}j} = k_{\mathrm{p}j} + k_{\mathrm{i}j}\tau_{\mathrm{d}j}$ and $\bar{k}_{\mathrm{i}j} = k_{\mathrm{i}j}$. The controller coefficients are then chosen by arbitrarily fixing the free design parameters ξ_{tj} and ω_{tj} to assign the modal damping and natural frequency of the closed loop, and then selecting

$$\bar{k}_{\mathrm{p}j} = \frac{\xi_j\omega_{tj}}{\xi_{tj}\omega_j}, \bar{k}_{\mathrm{i}j} = \frac{\omega_{tj}}{2\xi_{tj}}, \bar{k}_{\mathrm{d}j} = \frac{\omega_{tj}}{2\xi_{tj}\omega_j^2}, \tau_{\mathrm{d}j} = \frac{1}{2\xi_{tj}\omega_{tj}}. \tag{14}$$

In fact, by replacing (12) – (14) in (9), we obtain the desired closed-loop transfer function

$$\begin{aligned}\boldsymbol{T}_{\mathrm{r}\boldsymbol{j}} = \ & \frac{\omega_{\mathrm{t}j}^2}{s^2 + 2\xi_{\mathrm{t}j}\omega_{\mathrm{t}j}s + \omega_{\mathrm{t}j}^2}\boldsymbol{T}_{\mathrm{s}\boldsymbol{j}} - \\ & \frac{s^2(s + 2\xi_j\omega_j)(s + 2\xi_{\mathrm{t}j}\omega_{\mathrm{t}j})}{(s^2 + 2\xi_j\omega_j s + \omega_j^2)(s^2 + 2\xi_{\mathrm{t}j}\omega_{\mathrm{t}j}s + \omega_{\mathrm{t}j}^2)}\boldsymbol{T}_{\mathrm{d}\boldsymbol{j}} \\ = \ & G_j(s)\boldsymbol{T}_{\mathrm{s}\boldsymbol{j}} + H_j(s)\boldsymbol{T}_{\mathrm{d}\boldsymbol{j}}\end{aligned} \tag{15}$$

showing that the proposed controller successfully replaces the second-order open-loop dynamics $P_j(s)$, described by coefficients ω_j and ξ_j, with the target second-order closed-loop dynamics $G_j(s)$ corresponding to coefficients $\omega_{\mathrm{t}j}$ and $\xi_{\mathrm{t}j}$ freely specified by the designer. The effect of the disturbance $\boldsymbol{T}_{\mathrm{d}\boldsymbol{j}}$ is described by the transfer function $H_j(s)$. We refer to (15) as *closed loop* since it describes the system response when the low-level torque feedback in the blue block in Fig. 2 (right) is applied. The effects of the closed loop and our selection of parameters $\omega_{\mathrm{t}j}$ and $\xi_{\mathrm{t}j}$ are represented in Fig. 4 (bottom) in the frequency domain, showing that the resonance peak of $P_j(s)$ is completely attenuated in $G_j(s)$, while maintaining torque bandwidth larger than 10 Hz. By considering again the low-frequency limit case of (15), we obtain:

$$\boldsymbol{T}_{\mathrm{r}\boldsymbol{j}} \approx \boldsymbol{T}_{\mathrm{s}\boldsymbol{j}} + \left(2\xi_j\frac{\omega}{\omega_j}\right)\left(2\xi_{\mathrm{t}j}\frac{\omega}{\omega_{\mathrm{t}j}}\right)\boldsymbol{T}_{\mathrm{d}\boldsymbol{j}}. \tag{16}$$

The comparison between (16) and (10) shows that the low-frequency disturbance effect produced by the joint rotation can be further attenuated with respect to the open-loop case by increasing the closed-loop bandwidth $\omega_{\mathrm{t}j}$; this can be visualized in the parametric analysis of $H_j(s)$ in Fig. 5. From (14), we see that choosing a larger $\omega_{\mathrm{t}j}$ results in higher control gains. In practice, the control gains cannot be chosen arbitrarily large due to robustness requirements (e.g., due to the effect of neglected high-frequency dynamics).

To further investigate the low-frequency analysis of the proposed scheme, note that (15) implies that $T_{\mathrm{r}j}$ tightly follows $T_{\mathrm{s}j}$ as long as $G_j(j\omega)$ approaches the unit value and the magnitude of $H_j(j\omega)$ is small, namely:

$$|G_j(j\omega)| > 0.95 \quad \text{and} \quad |H_j(j\omega)| < 0.05. \tag{17}$$

Transfer functions $G_j(s)$ and $H_j(s)$ are shown in Fig. 4 (bottom) for experimental values of the model parameters and control gains, showing that the dynamic decoupling (17) holds in the range 0–6 Hz. In this range, the arm $\mathcal{S}$ can be actually controlled by neglecting the motor/transmission dynamics because $T_{\mathrm{r}j} \approx T_{\mathrm{s}j}$. When this approximation holds true, the differential equation for θ_r appearing in (6) can be approximated as

$$M_{\mathrm{r}}(\theta_{\mathrm{r}})\ddot{\theta}_{\mathrm{r}} + D_{\mathrm{r}}\dot{\theta}_{\mathrm{r}} + C_{\mathrm{r}}(\theta_{\mathrm{r}}, \dot{\theta}_{\mathrm{r}})\dot{\theta}_{\mathrm{r}} + G_{\mathrm{r}}(\theta_{\mathrm{r}}) = T_{\mathrm{s}} + J^{\top}(\theta_{\mathrm{r}})F. \tag{18}$$

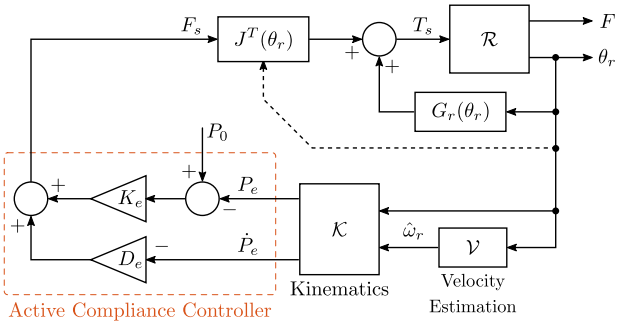

Fig. 6. High-level HRI controller for active compliance (stiffness and damping) assignment in the operational space.

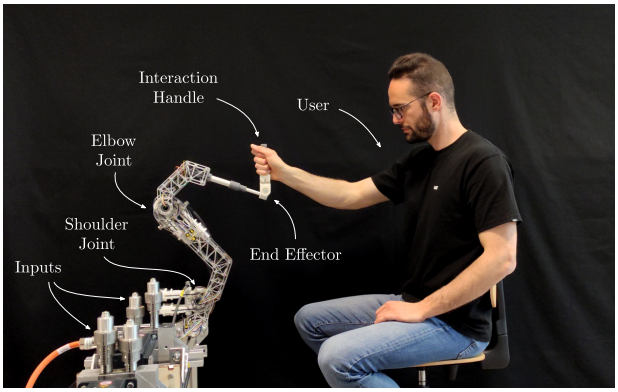

Fig. 7. Experimental setup (notice that the robot base is rotated by 90° in the photo in order to offer a clearer view of the setup, but all the tests are performed in the nominal configuration represented in Fig. 1). Please also see the videos attached as supplementary material.

where it is clear that T_s plays the same role as the generalized joint torque in conventional robot control schemes, and thus it can be used to directly control the robot motion/interaction behavior.

IV. High-level HRI Controller

In this section, we develop a high-level feedback control law which aims at shaping the human-robot interaction at the end-effector power port $F - \dot{P}_\mathrm{e}$. To this end, we consider the robot dynamics with pressure feedback loops, where the low-level controllers have been tuned such that (18) holds true in the low-frequency range. The high-level controller, represented in Fig. 6, operates by assigning the setpoint input T_s to the block $\mathcal{R}$ implementing the low-level scheme shown in Fig. 2 (right). Setpoint T_s is selected as an operating space PD with gravity compensation:

$$\begin{aligned} T_\mathrm{s} &= G_\mathrm{r}(\theta_\mathrm{r}) - J^\top(\theta_r) F_\mathrm{s}, \\ \text{with } F_\mathrm{s} &= K_\mathrm{e}(P_\mathrm{e}(\theta_\mathrm{r}) - P_0) + D_\mathrm{e} J(\theta_\mathrm{r})\dot{\theta}_\mathrm{r} \end{aligned} \tag{19}$$

where K_e and D_e are free design parameters corresponding to the virtual stiffness and damping matrices in the operating space, given by

$$K_\mathrm{e} = \begin{bmatrix} k_{ex} & 0 \\ 0 & k_{ey} \end{bmatrix} > 0, \quad D_\mathrm{e} = \begin{bmatrix} d_{ex} & 0 \\ 0 & d_{ey} \end{bmatrix} > 0, \tag{20}$$

while $P_0 = [P_{0x}, P_{0y}]^\top$ defines the contact-free virtual equilibrium position of the end-effector in the operating space. The actual end-effector position $P_\mathrm{e}(\theta_\mathrm{r})$ is computed from the direct kinematics, while the joint speed $\dot{\theta}_\mathrm{r}$ is estimated through measurements of θ_r by using high-pass filters, i.e.,

$$\mathcal{V} = \begin{bmatrix} v_1(s) & 0 \\ 0 & v_2(s) \end{bmatrix}, \quad v_j(s) = \frac{k_{\mathrm{f}j}\, s}{s + k_{\mathrm{f}j}}, \quad j = 1, 2 \tag{21}$$

where parameters k_{fj} define the filter cut-off frequencies (experimental settings: $k_{\mathrm{f}1} = k_{\mathrm{f}2} = 50$).

By replacing (19) into (18), the high-level closed-loop dynamics yields:

$$\begin{aligned} M_r(\theta_\mathrm{r})\ddot{\theta}_\mathrm{r} + D_r\dot{\theta}_\mathrm{r} + J^\top(\theta_\mathrm{r}) D_\mathrm{e} J(\theta_\mathrm{r})\dot{\theta}_\mathrm{r} + C_\mathrm{r}(\theta_\mathrm{r}, \dot{\theta}_\mathrm{r})\dot{\theta}_\mathrm{r} + \\ J^\top(\theta_\mathrm{r}) K_\mathrm{e}\left(P_\mathrm{e}(\theta_\mathrm{r}) - P_0\right) = J^\top(\theta_\mathrm{r}) F. \end{aligned} \tag{22}$$

It is observed that, in stationary conditions, (22) implies

$$J^\top(\theta_\mathrm{r}) K_\mathrm{e}\left(P_\mathrm{e}(\theta_\mathrm{r}) - P_0\right) = J^\top(\theta_\mathrm{r}) F, \tag{23}$$

and whenever we are in a non-singular configuration (i.e., $J(\theta_\mathrm{r})$ is full rank), (23) gives

$$K_\mathrm{e}\left(P_\mathrm{e}(\theta_\mathrm{r}) - P_0\right) = F, \tag{24}$$

which represents a linear elastic characteristics in the operating space. Quantities K_e and P_0 can then be interpreted as a virtual stiffness and a contact-free end-effector position in the operating space, respectively.

An attractive feature of control law (19) is that it makes the closed-loop system (22) passive at the end-effector port $F - \dot{P}_\mathrm{e}$ (see [23], Chapter 6). This can be proven by considering the storage function

$$H(\theta_\mathrm{r}, \dot{\theta}_\mathrm{r}) = \frac{1}{2}\dot{\theta}_\mathrm{r}^\top M_\mathrm{r}(\theta_\mathrm{r})\dot{\theta}_\mathrm{r} + \frac{1}{2}\left(P(\theta_\mathrm{r}) - P_0\right)^\top K_\mathrm{e}\left(P(\theta_\mathrm{r}) - P_0\right). \tag{25}$$

Differentiating (25) along dynamics (22), and recalling the skew-symmetry of matrix $\dot{M}_\mathrm{r}(\theta_\mathrm{r}) - 2C_\mathrm{r}(\theta_\mathrm{r}, \dot{\theta}_\mathrm{r})$ (see [22], Chapter 7), we obtain

$$\begin{aligned} \dot{H} &= -\dot{\theta}_\mathrm{r}^\top D_\mathrm{r}\dot{\theta}_\mathrm{r} - \dot{\theta}_\mathrm{r}^\top J^\top(\theta_\mathrm{r}) D_\mathrm{e} J(\theta_\mathrm{r})\dot{\theta}_\mathrm{r} + \dot{\theta}_\mathrm{r}^\top J^\top(\theta_\mathrm{r}) F \\ &= -\dot{\theta}_\mathrm{r}^\top D_\mathrm{r}\dot{\theta}_\mathrm{r} - \dot{P}_\mathrm{e}^\top D_\mathrm{e}\dot{P}_\mathrm{e} + \dot{P}_\mathrm{e}^\top F \\ &\leq \dot{P}_\mathrm{e}^\top F, \end{aligned} \tag{26}$$

which is indeed the well-known passivity inequality. The above discussed passivity property allows us to state that the manipulator will remain stable whenever its end-effector interacts with an external passive system (such as a human operator), as long as K_e and D_e are chosen according to (20), [24]. This property makes the developed architecture particularly suitable for safe interaction control with unstructured systems and environments. In addition, the second line in (26) shows that D_e permits to directly assign the damping in the operating space.

V. Experiments

This section demonstrates the effectiveness of the proposed human-friendly robotic arm in a human-robot-interaction experimental setup where the robot is operated by the human user through the end-effector handle. To suitably assess both the mechanical and control design paradigms, our experiments

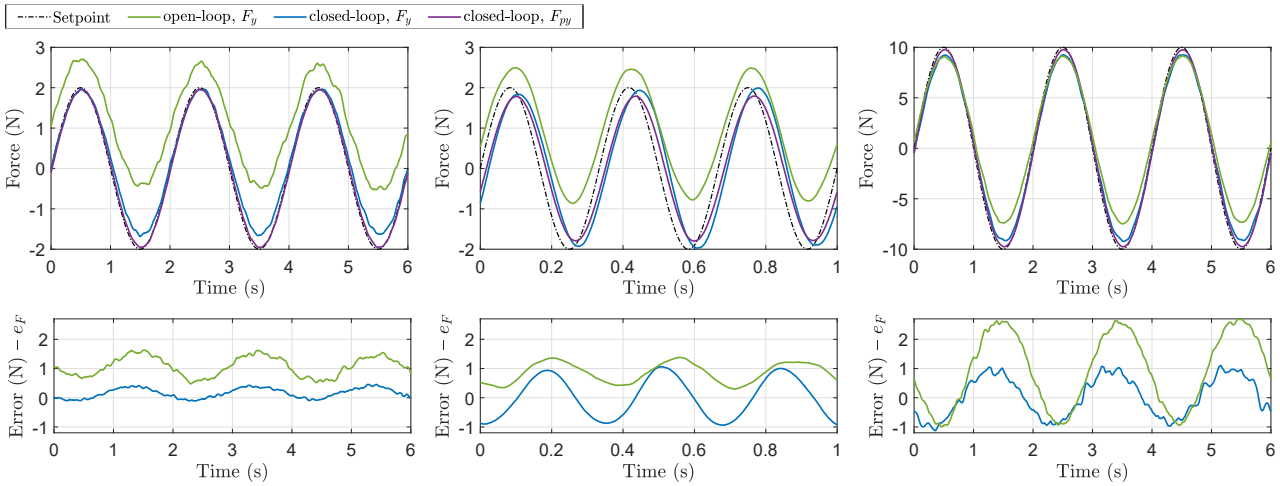

Fig. 8. Sine tracking experiment. The human user holds the handle at a fixed position and a sinusoidal force reference (dashed-dotted black line) is tracked at the end effector along the y direction. The green line and the blue line represent the load cell measurement in the open-loop and closed-loop configurations, respectively. The purple line represents the output force measured by means of the pressure sensors in the closed-loop case. *Left:* low-amplitude low-frequency test ($A = 2$ N, $\omega = 0.25$ Hz); *Center:* increased setpoint frequency ($A = 2$ N, $\omega = 3$ Hz); *Right:* increased setpoint amplitude ($A = 10$ N, $\omega = 0.25$ Hz).

are carried out both with the open-loop configuration (9) and with the pressure-based closed-loop configuration (15).

A. Sine Tracking without Compliance Controller

First, the force tracking capability of the robotic arm is assessed by asking the human operator to hold the handle at a fixed position and by opening the outer loop in Fig. 6 assessing the desired operating-space force F_{s} in (19) as

$$F_{\mathrm{s}} = \begin{bmatrix} 0 \\ A sin\left(2\pi f t\right) \end{bmatrix} \tag{27}$$

where constant A is the setpoint amplitude and constant f is the setpoint frequency. In this configuration, the active compliance controller in Fig. 6 is disabled. The results are shown in Fig. 8. A first low-amplitude ($A = 2$ N) and low-frequency ($f = 0.25$ Hz) test is reported in the left plot, which compares the measurement of the second component F_y of the force output F produced in the open-loop (green line) and closed-loop (blue line) configurations (9) and (15) , respectively. The tracking error, which reaches a maximum value of 1.6 N in the open-loop experiment, is consistently reduced in the closed-loop experiment (max. 0.45 N), where the action of the low-level controller removes the residual bias affecting the output of the open-loop response (possibly caused by imperfections and/or residual spring-rate effects in the rolling diaphragms), and ensures a closer match with the setpoint (dashed-dotted black line). The purple line shows the measurement of the output force by means of the pressure sensors F_{py} for the closed-loop experiment: this measurement closely matches the setpoint and well represents the actual output force F_y measured by the load cell sensor, which is not used for the feedback action: it is only used as ground truth measurement for validation purposes. Similar conclusions can be drawn when repeating the test with a larger setpoint frequency $f = 3$ Hz in Fig. 8 (center), and with a larger setpoint amplitude $A = 10$ N in Fig. 8 (right), testifying that the accuracy of the robot is preserved for faster velocities and higher loads.

B. Backdrivability without Compliance Controller

The response of the robot is further investigated by means of backdrivability tests that, differently from previous experiments, take into account large displacements. The reference force F_{s} in (19) is set to zero by selecting the virtual damping $D_{\mathrm{e}} = 0$ and virtual stiffness $K_{\mathrm{e}} = 0$ in active compliance controller (19). The human imposes vertical and horizontal end-effector displacements with an amplitude of 150 mm, as shown in Fig. 9 (left), about different nominal postures of the manipulator, in order to assess the accuracy/transparency of the robot in different positions and direction. Fig. 9 (center) and Fig. 9 (top-right) show the load-cell output measurement $F = [F_x, F_y]^\top$ during low-velocity displacements along the y and x directions, respectively: in each plot, colors are used to associate the force measurement with the corresponding trajectory shown in the left picture, while the line style is used to distinguish between the open-loop (dashed lines, system (9)) and closed-loop (solid lines, system (15)) responses. The mean value was subtracted from each position measurement in the force-displacement plots, in order to overlap plots that are actually located in different positions of the workspace, as shown in Fig. 9 (left). The effect of the low-level controller is again clearly visible in these tests, where the closed loop is significantly more accurate and transparent than the open loop, resulting in a smaller force required by the user to backdrive the robot in all the experiments: as compared to the open loop, the maximum effort is reduced from 3 N to 1.6 N (worst case values) and the measurements performed in the closed-loop configuration (15) are more repeatable. Also notice how the output is influenced by the posture of the robot: when the arm is extended (purple posture) the highest accuracy is obtained with the vertical displacements (y direction, central plot), while, when the arm is contracted (green posture), the highest accuracy is obtained with the

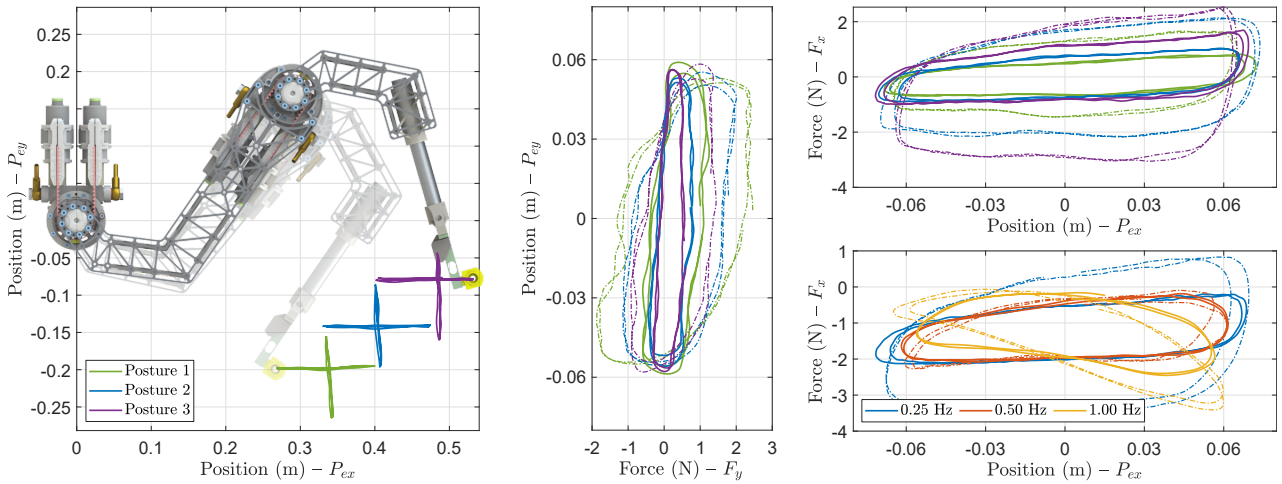

Fig. 9. Backdrivability test. F_s is set to zero, while the user imposes a displacement at the end-effector (150 mm amplitude and 0.25 Hz frequency) along the x and y directions. Different colors refer to different nominal postures of the robot, while different line styles refer to the control configuration (solid lines for the closed loop, dashed lines for the open loop). *Left:* vertical and horizontal trajectories performed about 3 different reference postures; *Center*: force F_y measured during the vertical displacements; *Top-right*: force F_x measured during the horizontal displacements; *Bottom-right*: the horizontal test about posture 2 is repeated with different frequencies.

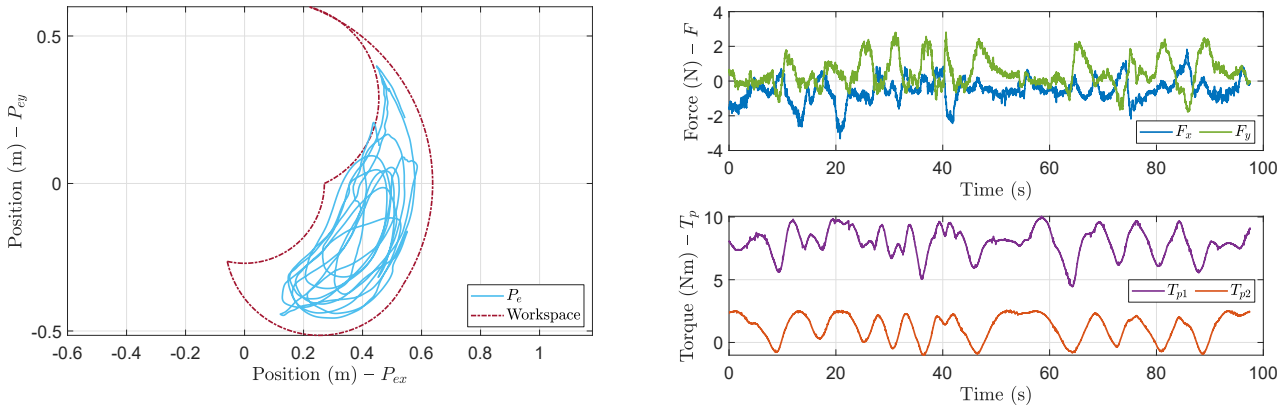

Fig. 10. Backdrivability test with an additional 1.5 kg payload fixed close to the end-effector. *Left*: trajectory imposed at the end-effector by the user (light-blue line) covering a large portion of the reachable workspace (dashed-dotted red line); *Top-right*: end-effector force components F_x and F_y measured by the load-cell; *Bottom-right:* torque profiles of the shoulder and elbow joints.

horizontal displacements (x direction, top-right plot). In this last case, the purple measurement actually corresponds to the worst performance. This confirms the fact that a fully extended planar arm loses controllability along the direction perpendicular to the arm itself, and that the controllability along that direction is gradually restored as the elbow joint bends. Finally, Fig. 9 (bottom-right) shows the backdrivability properties with higher velocities: additional tests about posture 2 are performed by increasing the displacement frequency at each repetition, ranging from 0.25 Hz to 1 Hz. The maximum effort required for the user to backdrive the robot does not show a clear dependence on the velocity in the current experimental conditions and, in general, the closed-loop measurements are once again more repeatable that the open-loop ones. This set of high-speed tests (characterised by an end-effector maximum velocity of 0.42 m/s and an elbow-joint maximum velocity of 1.64 rad/s) probably highlights the most relevant difference between the proposed architecture, i.e. direct drive motorization remotized by means of transmission systems, and a common industrial highly-geared robotic joint, where the former is capable of easily preserving accuracy and transparency features at high velocities.

A further backdrivability test is shown in Fig. 10, where a payload of 1.5 kg is applied in the proximity of the end effector and its weight was suitably taken into account in the control law by an appropriate gravity compensation term. The user imposes a generic motion of the end effector covering almost the entire extension of the reachable workspace, as shown in Fig. 10 (left). The interaction force $F = [F_x, F_y]^\top$ measured at the user hand, shown in Fig. 10 (top-right), remains within the expected limit values measured in the previous standard backdrivability experiments, never requiring the user to apply larger forces than 3 N to backdrive the robot. The response is reasonably transparent and uniform over the entire workspace even when the transmission is heavily loaded: in particular, Fig. 10 (bottom-right) shows the torque profile of the two joints recorded during the experiment, revealing an average working torque of about 8 Nm, reaching peak values of 10 Nm

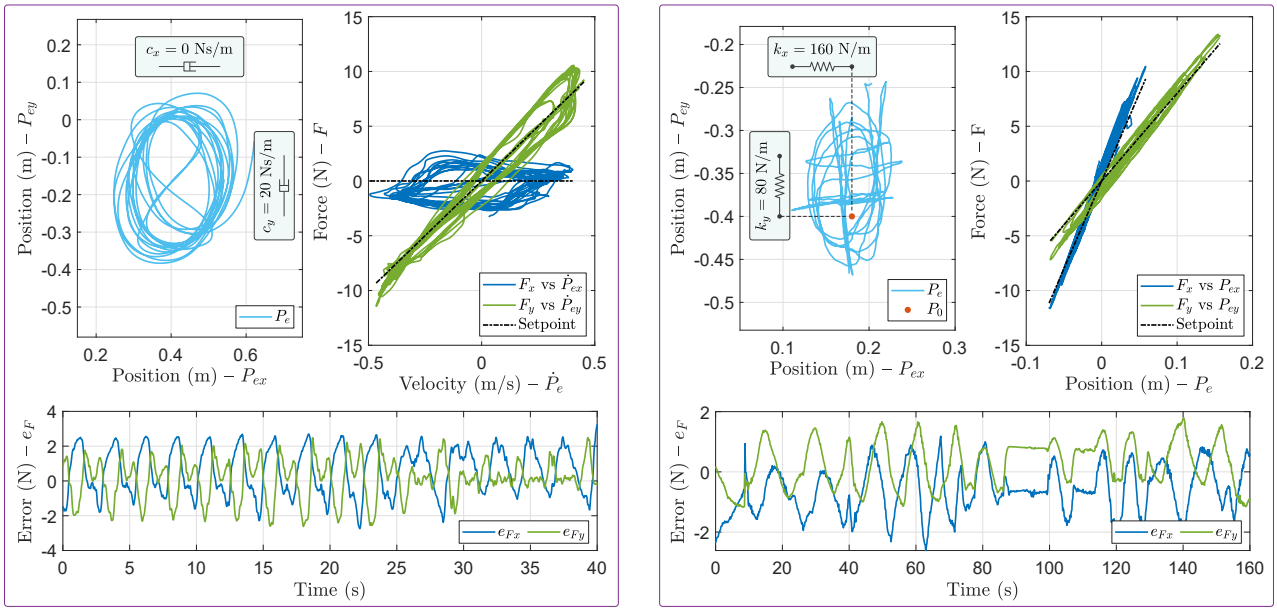

Fig. 11. Experimental assessment of the high-level compliance controller of Fig. 6: the user imposes arbitrary trajectories at the end-effector (light blue lines) while the robot opposes to the motion of the user hand by applying (*Left*) an artificial viscous action and (*Right*) an artificial elastic reaction (the red dot indicates the virtual equilibrium position P_0 in (19)). Different damping/stiffness coefficients are chosen for the x and y axes: $d_{ex} = 0$ Ns/m and $d_{ey} = 20$ Ns/m in the first test, while of $k_{ex} = 160$ N/m and $k_{ey} = 80$ N/m in the second test. In both plots, the *top-left* picture shows the interaction handle position; the *top-right* picture plots the components of both the force reference F_s (black lines) and the actual interaction force F (colored lines) with respect to the corresponding displacement/velocity component; the *bottom* picture show the components of the force tracking error $e_F = F_s - F$.

at the shoulder joint.

C. Testing the High-level Compliance Controller

Finally, the overall control architecture of Fig. 6 and (19) is tested in human-robot-interaction experiments requiring the robot to display the virtual compliance, by associating artificial viscous or elastic forces with the movement of the user hand. Two set of experiments are performed, the first one in Fig. 11 (left) with pure damping assignment ($K_e = 0$ in (19)) and the second one in Fig. 11 (right) with pure stiffness assignment ($D_e = 0$ in (19)). K_e and D_e are selected diagonal in (19) and different damping/stiffness coefficients are specified along the x and y axes, in order to challenge the robot to exhibit sufficiently rich compliance action. $K_e = 0$ N/m and $D_e = \text{diag}(0, 20)$ Ns/m are selected for the damping experiment while $K_e = \text{diag}(160, 80)$ N/m and $D_e = 0$ Ns/m are selected for the stiffness experiments. Both tests show similar tracking errors (bottom plots of Fig. 11) along the x and y axes, highlighting a desirable uniform force tracking accuracy over a range of different load intensities along the two axes. This result also testifies a good decoupling of the force controllability performance along the two axes. Consistently with the results of Fig. 9, a maximum error of 2.7 N is measured in the first test, and a maximum error of 2.5 N is measured in the second one.

VI. Conclusions

This work addressed the simultaneous development of a novel mechanical and control approach for human-friendly robotic arms. Hydrostatic transmissions based on low-friction rolling diaphragm cylinders allow for remote positioning of the electric actuators, thus providing lightweight robotic arms with enhanced dynamical properties. A multi-loop controller based on pressure feedback ensures stable closed-loop force setpoint regulation with arm-transmission dynamics decoupling up to 6 Hz and structural resonance attenuation. Experimental tests show that the closed loop increases the backdrivability and the force tracking accuracy in a variety of experimental conditions. The maximum measured backdriving force at the end-effector is equal to 3 N in open loop and 1.6 N in closed loop. The lightweight robotic arm proved also powerful in a collaborative experiment by helping the user to carry a payload of 1.5 kg across its entire workspace, while maintaining uniform interaction transparency features over the whole operating range. The robot backdrivability did not degrade in heavy load tasks, proving that the frictional and dynamical properties of hydrostatic transmissions are independent of the applied load; this is a significant advantage with respect to existing cable-based transmissions or similar solutions. Complex human-machine-interaction tasks involving the display of virtual stiffness and damping assignment have been accomplished with high accuracy.

VII. Supplementary Material

Two videos showing experimental interaction between the prototype and a human user are provided as additional material.

"TRO-hydrostatic-transmission-backdriveable" shows the robot's pure backdrivability response, experimentally characterized in a similar way in Sect. V-B.

"TRO-hydrostatic-transmission-haptic" extends the haptic display of elastic and damping forces, characterised in

Sect. V-C, to simulate the interaction of the user with a virtual wall. This experiment is not intended as a rigorous characterisation of the haptic rendering performance of the device.

REFERENCES

[1] G. Hirzinger, A. Albu-Schaffer, M. Hahnle, I. Schaefer, and N. Sporer, "On a new generation of torque controlled light-weight robots," in *Proceedings 2001 ICRA. IEEE International Conference on Robotics and Automation (Cat. No. 01CH37164)*, vol. 4. IEEE, 2001, pp. 3356–3363.

[2] G. A. Pratt and M. M. Williamson, "Series elastic actuators," in *Proceedings 1995 IEEE/RSJ International Conference on Intelligent Robots and Systems. Human Robot Interaction and Cooperative Robots*, vol. 1. IEEE, 1995, pp. 399–406.

[3] B. Vanderborght, A. Albu-Schäffer, A. Bicchi, E. Burdet, D. G. Caldwell, R. Carloni, M. Catalano, O. Eiberger, W. Friedl, G. Ganesh *et al.*, "Variable impedance actuators: A review," *Robotics and autonomous systems*, vol. 61, no. 12, pp. 1601–1614, 2013.

[4] K. Salisbury, W. Townsend, B. Ebrman, and D. DiPietro, "Preliminary design of a whole-arm manipulation system (wams)," in *Proceedings. 1988 IEEE International Conference on Robotics and Automation*. IEEE, 1988, pp. 254–260.

[5] A. Frisoli, F. Salsedo, M. Bergamasco, B. Rossi, and M. C. Carboncini, "A force-feedback exoskeleton for upper-limb rehabilitation in virtual reality," *Applied Bionics and Biomechanics*, vol. 6, no. 2, pp. 115–126, 2009.

[6] S. Grosu, L. De Rijcke, V. Grosu, J. Geeroms, B. Vanderboght, D. Lefeber, and C. Rodriguez-Guerrero, "Driving robotic exoskeletons using cable-based transmissions: a qualitative analysis and overview," *Applied Mechanics Reviews*, vol. 70, no. 6, 2018.

[7] J. P. Whitney, T. Chen, J. Mars, and J. K. Hodgins, "A hybrid hydrostatic transmission and human-safe haptic telepresence robot," in *2016 IEEE international conference on robotics and automation (ICRA)*. IEEE, 2016, pp. 690–695.

[8] S. Frishman, R. D. Ings, V. Sheth, B. L. Daniel, and M. R. Cutkosky, "Extending reach inside the mri bore: A 7-dof, low-friction, hydrostatic teleoperator," *IEEE Transactions on Medical Robotics and Bionics*, vol. 3, no. 3, pp. 701–713, 2021.

[9] S. Frishman, A. Kight, I. Pirozzi, M. C. Coffey, B. L. Daniel, and M. R. Cutkosky, "Enabling in-bore mri-guided biopsies with force feedback," *IEEE transactions on haptics*, vol. 13, no. 1, pp. 159–166, 2020.

[10] N. Burkhard, S. Frishman, A. Gruebele, J. P. Whitney, R. Goldman, B. Daniel, and M. Cutkosky, "A rolling-diaphragm hydrostatic transmission for remote mr-guided needle insertion," in *2017 IEEE international conference on robotics and automation (ICRA)*. IEEE, 2017, pp. 1148–1153.

[11] M. Bolignari, G. Moretti, and M. Fontana, "Design and Experimental Characterisation of a Hydrostatic Transmission for Upper Limb Exoskeletons," in *2018 IEEE/RSJ International Conference on Intelligent Robots and Systems (IROS)*, 2018.

[12] C. Khazoom, C. Véronneau, J.-P. L. Bigué, J. Grenier, A. Girard, and J.-S. Plante, "Design and control of a multifunctional ankle exoskeleton powered by magnetorheological actuators to assist walking, jumping, and landing," *IEEE Robotics and Automation Letters*, vol. 4, no. 3, pp. 3083–3090, 2019.

[13] C. Véronneau, J.-P. L. Bigué, A. Lussier-Desbiens, and J.-S. Plante, "A high-bandwidth back-drivable hydrostatic power distribution system for exoskeletons based on magnetorheological clutches," *IEEE Robotics and Automation Letters*, vol. 3, no. 3, pp. 2592–2599, 2018.

[14] C. Véronneau, J. Denis, L.-P. Lebel, M. Denninger, V. Blanchard, A. Girard, and J.-S. Plante, "Multifunctional remotely actuated 3-dof supernumerary robotic arm based on magnetorheological clutches and hydrostatic transmission lines," *IEEE Robotics and Automation Letters*, vol. 5, no. 2, pp. 2546–2553, 2020.

[15] C. Véronneau, J. Denis, L.-P. Lebel, M. Denninger, J.-S. Plante, and A. Girard, "A lightweight force-controllable wearable arm based on magnetorheological-hydrostatic actuators," in *2019 international conference on robotics and automation (ICRA)*. IEEE, 2019, pp. 4018–4024.

[16] C. Khazoom, P. Caillouette, A. Girard, and J.-S. Plante, "A supernumerary robotic leg powered by magnetorheological actuators to assist human locomotion," *IEEE Robotics and Automation Letters*, vol. 5, no. 4, pp. 5143–5150, 2020.

[17] E. Schwarm, K. M. Gravesmill, and J. P. Whitney, "A floating-piston hydrostatic linear actuator and remote-direct-drive 2-dof gripper," in *2019 international conference on robotics and automation (ICRA)*. IEEE, 2019, pp. 7562–7568.

[18] M. Bolignari, A. Mo, M. Fontana, and A. Badri-Spröwitz, "Diaphragm Ankle Actuation for Efficient Series Elastic Legged Robot Hopping," in *in-print 2022 IEEE/RSJ International Conference on Intelligent Robots and Systems (IROS)*, https://doi.org/10.48550/arXiv.2203.01595, 2022.

[19] J. P. Whitney, M. F. Glisson, E. L. Brockmeyer, and J. K. Hodgins, "A low-friction passive fluid transmission and fluid-tendon soft actuator," in *2014 IEEE/RSJ international conference on intelligent robots and systems*. IEEE, 2014, pp. 2801–2808.

[20] M. Bolignari and M. Fontana, "Design and experimental characterization of a high performance hydrostatic transmission for robot actuation," *Meccanica*, 2020.

[21] M. Bolignari, G. Rizzello, L. Zaccarian, and M. Fontana, "Smith-predictor-based torque control of a rolling diaphragm hydrostatic transmission," *IEEE Robotics and Automation Letters*, vol. 6, no. 2, pp. 2970–2977, 2021.

[22] B. Siciliano, L. Sciavicco, L. Villani, and G. Oriolo, "Robotics: Modelling, planning and control," 2010.

[23] H. K. Khalil, "Nonlinear systems third edition," *Patience Hall*, vol. 115, 2002.

[24] N. Hogan and S. P. Buerger, "Impedance and interaction control," in *Robotics and automation handbook*. CRC press, 2018, pp. 375–398.

Marco Bolignari was born in Florence, Italy, in 1992. He received the Ph.D. degree in Mechatronics Engineering from the University of Trento, Italy, in 2022. In 2021, he was a Visiting Researcher at the Dynamic Locomotion Group at the Max Planck Institute for Intelligent Systems, Stuttgart, Germany. In 2022 he joined the Institute of Mechanical Intelligence at the Scuola Superiore Sant'Anna, Pisa, Italy, as a Postdoctoral Researcher. His main research interests include the development of innovative mechanisms for industrial and medical robots.

Gianluca Rizzello (M'16) was born in Taranto, Italy, in 1987. He received the master's (Hons.) degree in control engineering from the Polytechnic University of Bari, Bari, Italy, in 2012. He received his Ph.D. in Information and Communication Technologies from Scuola Interpolitecnica di Dottorato, a joint program between Polytechnic Universities of Torino, Bari, and Milano, Italy, in 2016. After his doctoral studies, he joined the Saarland University, Saarbrücken, Germany, first with the role of a post-doc researcher and Group Leader Smart Material Modeling and Control (2016-2019), and subsequently as Assistant Professor in Adaptive Polymer Systems (2020 - present). His research interests involve modeling, control, and self-sensing of innovative mechatronic and robotic systems based on unconventional drive technologies, such as smart materials.

Luca Zaccarian (Fellow, IEEE) received the Ph.D. degree in computer and control engineering from the University of Roma Tor Vergata (Italy) in 2000, respectively. From 2000 to 2011 he has been Assistant Professor and then Associate Professor at that same university. Since 2011 he is Directeur de Recherche at the LAAS-CNRS, Toulouse (France) and since 2013 he holds a part-time professor position at the University of Trento, Italy. Luca Zaccarian's main research interests include analysis and design of nonlinear and hybrid control systems, modeling and control of mechatronic systems. He was a recipient of the 2001 O. Hugo Schuck Best Paper Award given by the American Automatic Control Council.

Marco Fontana received the master degree in Mechanical Engineering from University of Pisa in 2003 and the Ph.D. degree in Robotics from Scuola Superiore Sant'Anna (Italy) in 2008. From 2008 to 2016 he has been Post Doc and Assistant Professor same university. From 2016 to 2020 he has been Assistant and Associate Professor at the University of Trento. Since 2020 he holds an Associate Professor position in Mechanical Engineering at Scuola Superiore Sant'Anna, Italy, where he leads where he leads the group of *Robotic Mechanisms and Materials*. His main research interests are focussed on the development and optimization of innovative hardware solutions for advanced robots, mechatronic systems and energy harvesters.